PNAS RESEARCH ARTICLE | NEUROSCIENCE

Rapid synaptic and gamma rhythm signature of mouse critical period plasticity

Kathleen B. Quast[a,b,1], Rebecca K. Reh[a,b,1,2], Maddalena D. Caiati[a], Nancy Kopell[c,d,3], Michelle M. McCarthy[c,d,3], and Takao K. Hensch[a,b,d,3]

Contributed by Nancy Kopell; received December 24, 2021; accepted November 29, 2022; reviewed by Ralf A. Galuske and Tommaso Pizzorusso

Early-life experience enduringly sculpts thalamocortical (TC) axons and sensory processing. Here, we identify the very first synaptic targets that initiate critical period plasticity, heralded by altered cortical oscillations. Monocular deprivation (MD) acutely induced a transient (<3 h) peak in EEG γ-power (~40 Hz) specifically within the visual cortex, but only when the critical period was open (juvenile mice or adults after dark-rearing, *Lynx1*-deletion, or diazepam-rescued GAD65-deficiency). Rapid TC input loss onto parvalbumin-expressing (PV) inhibitory interneurons (but not onto nearby pyramidal cells) was observed within hours of MD in a TC slice preserving the visual pathway – again once critical periods opened. Computational TC modeling of the emergent γ-rhythm in response to MD delineated a cortical interneuronal gamma (ING) rhythm in networks of PV-cells bearing gap junctions at the start of the critical period. The ING rhythm effectively dissociated thalamic input from cortical spiking, leading to rapid loss of previously strong TC-to-PV connections through standard spike-timing-dependent plasticity rules. As a consequence, previously silent TC-to-PV connections could strengthen on a slower timescale, capturing the gradually increasing γ-frequency and eventual fade-out over time. Thus, ING enables cortical dynamics to transition from being dominated by the strongest TC input to one that senses the statistics of population TC input after MD. Taken together, our findings reveal the initial synaptic events underlying critical period plasticity and suggest that the fleeting ING accompanying a brief sensory perturbation may serve as a robust readout of TC network state with which to probe developmental trajectories.

thalamocortical | parvalbumin | oscillation | *Lynx1* | GAD65

Significance

Critical periods are developmental windows of rapid plasticity and remodeling of brain networks, whose trajectories are not yet fully understood. Here, we identify transient γ-oscillations induced by sensory imbalance in the mouse visual cortex as a signature of rapid TC plasticity, only when these windows are open. Using computational modeling, we explain the origin of these transient γ-rhythms and their role in rewiring TC networks to initiate the precritical to critical period transition. These findings offer a robust noninvasive biomarker of open critical period state with which to probe derailed trajectories of brain development.

Dramatic circuit reorganization is a hallmark of early critical periods (CP) in brain development. Thalamocortical (TC) axon morphology is notably sculpted in response to sensory deprivation. A classic example is the eventual shrinkage of ocular dominance "columns" in the primary visual cortex (V1) to an eye deprived of vision (1). Strikingly, these wholesale arbor changes are slow, and synaptic bouton alterations within them scale with TC arbor size over days of deprivation (2–4). Likewise, the pruning and regrowth of dendritic spines on excitatory pyramidal cells reflect slow proteolytic processes that gradually accumulate over days of monocular deprivation (MD) in parallel with the loss of visual acuity and responsiveness in mice (5, 6). Surprisingly, extracellular spike recordings suggest middle layers of V1 are the least plastic after MD (7, 8). Whether thalamo-recipient layer IV networks are merely passive transmitters of sensory input or play a more decisive role in sculpting higher level cortical networks during the CP therefore remains unresolved.

Local γ-aminobutyric acid (GABA) circuit maturation instead triggers the opening of sensory CPs, which can be manipulated by molecular and genetic factors (9–18). Fast-spiking, parvalbumin-expressing (PV) interneurons in supragranular cortical layers can shift their responsiveness earlier than pyramidal cells within one day of MD (10–12). Such early changes are consistent with the importance of PV-cell network maturation in initiating CP states (9). Notably, PV-cells also play a pivotal role in the generation of γ-band neuronal oscillatory activity (19) and spike-time coordination (20). The emergence of γ-activity in V1 is both age- and experience dependent, maturing at the onset of the ocular dominance CP (21). Here, we reveal a decreased TC synaptic input specifically onto PV+ interneurons in layer IV as the earliest synaptic changes found to date in response to MD. Using mathematical modeling, we further elucidate the likely processes underlying those early changes.

Electroencephalogram (EEG) recording immediately after acute sensory manipulations showed a rapid rise in γ-power that correlated with the open CP state, both in juvenile wild-type (WT) mice and in multiple models of shifted plastic windows. The brief peak in γ-power emerged immediately following MD, gradually rising in frequency and eventually fading out after several hours. To reveal the synaptic consequences of this rapid rise

Author contributions: N.K., M.M.M., and T.K.H. designed research; K.B.Q., R.K.R., M.D.C., and M.M.M. performed research; K.B.Q., R.K.R., and M.D.C. analyzed data; and K.B.Q., R.K.R., M.D.C., N.K., M.M.M., and T.K.H. wrote the paper.

Reviewers: R.A.G., Technische Universitat Darmstadt; and T.P., CNR / Scuola Normale Superiore (Pisa).

The authors declare no competing interest.

[1]K.B.Q. and R.K.R. contributed equally to this work.

[2]Present address: Department of Psychology, University of British Columbia, Vancouver, BC V6T 1Z4, Canada.

[3]To whom correspondence may be addressed. Email: nk@bu.edu, mmccart@bu.edu, or hensch@mcb.harvard.edu.

This article contains supporting information online at https://www.pnas.org/lookup/suppl/doi:10.1073/pnas.2123182120/-/DCSupplemental.

Published January 4, 2023.

in γ-power, we optimized a TC slice preparation (22) to directly probe thalamic input onto PV+ and pyramidal cells in layer IV of V1 following deprivation. A dramatic decrease in thalamic input onto PV-cells within layer IV was seen as soon as 2 h after MD, while the same input onto nearby pyramidal cells was unchanged. In order to explore the possibility of a functional relationship between the immediate γ-oscillations and the loss of TC-to-PV synaptic strength post-MD, we turned to mathematical modeling of TC circuits.

We hypothesized that an imbalance in excitatory input onto PV-cells following MD, only during the CP, may initiate ING (interneuronal gamma) rhythms that drive plastic changes associated with the effects of MD. PV-cells are known to self-organize to produce an ING when electrical coupling as well as mutual inhibitory connections are present (19, 20). The developmental trajectory of electrical and inhibitory connections between PV-cells coincides with the onset of CP opening (8, 23) suggesting ING networks are functional during the CP. Our models confirm that γ-oscillations readily emerge through cortical ING dynamics during CP states in response to imbalanced thalamic input, and functionally alter the spike timing between TC cells and PV neurons leading to weakening of previously strong TC-to-PV connections. On a slower timescale, our models predict that ING initiates strengthening of previously silent TC-to-PV synaptic connections, causing the rising γ-frequency and eventual fade out of these oscillations observed experimentally.

Over the time course of MD-induced γ-rhythms, the TC-to-PV network transitions from being independent of input statistics to highly dependent on input statistics. Our study identifies the initial synaptic events driven by MD that precede by days the well-known, anatomical TC axonal arbor changes (1–4). Moreover, the concomitant rise in γ-power holds exciting promise as a robust, rapid biomarker of CP state in humans.

Results

Deprivation Triggers a Rapid, Transient Rise in γ-Power Only During the CP. We recorded the EEG from V1 in awake, behaving mice immediately following eyelid closure. In young WT (postnatal day P24-27), a rapid rise in oscillatory activity was observed selectively in the γ-frequency band, centered at 42 Hz (Fig. 1 and *SI Appendix*, Fig. S1). The power increase was transient, rising over the first 20 min post-MD and abating by 2 h (mean duration ± SD = 93 ± 22 min; Fig. 1*B*) – a striking immediate signature of deprivation during the CP. To rule out the impact of isoflurane exposure during the suturing procedure, control animals underwent anesthesia without eyelid suture. No peak in γ-power was observed in this group (mean maximum γ-power for no MD = 0.11 ± 0.04, 12 mice; MD = 0.32 ± 0.05, 14 mice; Figs. 1 *B* and *C* and 2*A*).

Notably, γ-power was not elevated indiscriminately across the brain, as somatosensory cortex recordings showed no increase in γ-power following MD (mean maximum γ-power over S1 = 0.10 ± 0.01, 9 mice; Figs. 1*D* and 2*A*). To determine whether γ-power elevation was driven by sensory input, some mice were immediately placed in a dark chamber after eyelid closure. EEG recordings from V1 commenced 10 min later after recovery from anesthesia in the dark and did not differ from nonsutured controls (mean maximum γ-power for MD in darkness = 0.15 ± 0.02, 10 mice; Fig. 1*E*). Together, these results indicate an imbalanced visual input during the CP leads to a rapid rise in rhythmic activity selectively in V1. To further investigate whether this brief γ-peak is restricted to a plastic window, we recorded EEG from older mice (>P90). There was no difference in γ-power between these adult animals receiving MD and anesthesia only controls (mean maximum γ-power no MD = 0.176 ± 0.021, 10 mice; MD = 0.175 ± 0.037, 12 mice; Fig. 2*A*).

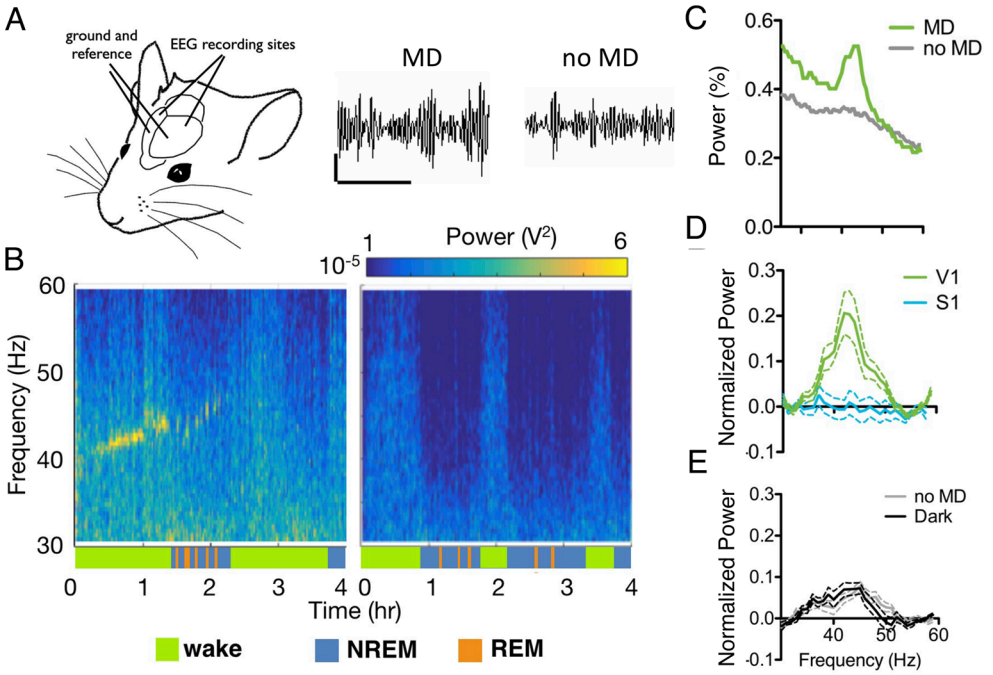

Fig. 1. Monocular deprivation induces a peak in γ rhythm (~40 Hz) during the CP. (*A*) EEG electrodes placed on the surface of the cortex bilaterally over V1, with ground and reference placed anteriorly. EEG traces from V1 with or without MD, band-pass filtered between 30 and 60 Hz. (Scale bar: 200 mV, 500 ms.) (*B*) EEG power spectrum from representative wt juvenile mice following MD (*Left*) or anesthesia (*Right*). Behavioral state indicated by colored bars below plots. (*C*) Average power spectrum during wake for the first 2 h following anesthesia comparing the two mice shown in *B*, as a percentage of total power. (*D*) Mean γ power over V1 for the first hour post-MD (green, n = 14), MD with EEG over S1 (blue, n = 9); *(E)* no MD (gray, n=12) or MD recorded in darkness (black, n = 10). Normalized to NREM γ power, error bars show SEM.

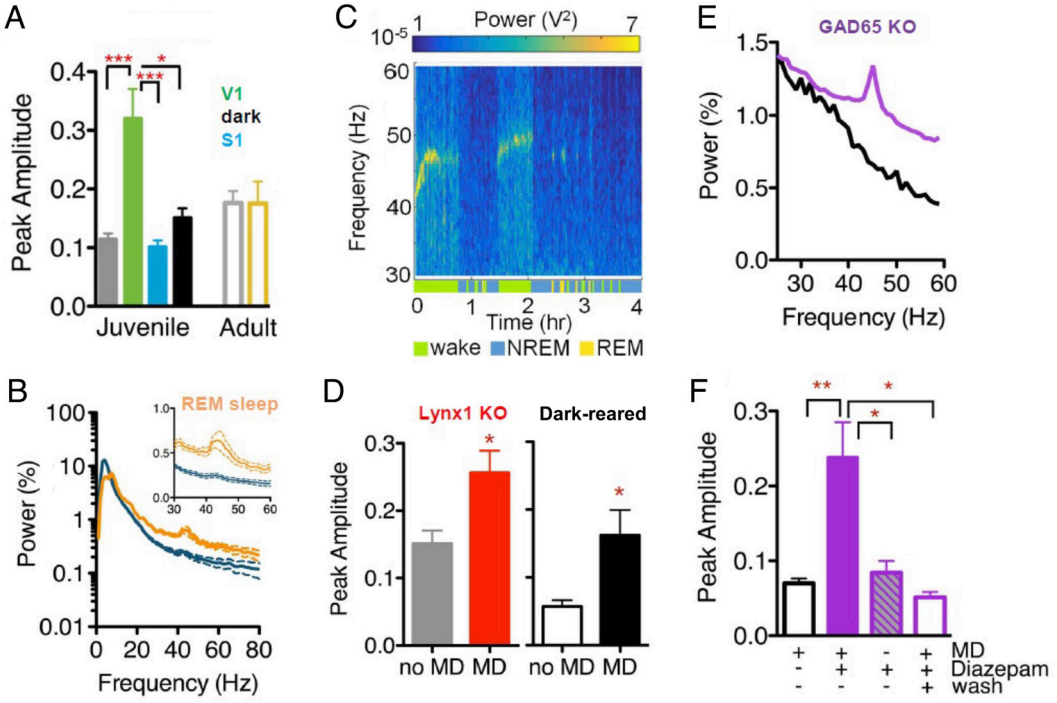

Fig. 2. γ power rise reflects level of adult plasticity. (*A*) The mean maximal γ power amplitude, comparing juvenile wt mice following MD (green, *n* = 14), no MD (gray, *n* = 12), MD with EEG over S1 (blue, *n* = 9), and MD recorded in darkness (black, *n* = 10; 1-way ANOVA with Tukey's Comparison, **P* < 0.05, *** *P* < 0.001), or adult wt mice following no MD (gray, *n* = 10) or MD (yellow, *n* = 12; Mann–Whitney test, *P* = 0.1065). (*B*) Mean NREM (blue) and REM (orange) power spectra of juvenile wt mice in the first 2 h following MD, shown as total percentage of power. Insert expands low γ band region. (*C*) EEG power spectrum from representative adult *Lynx1* KO mouse following MD, with behavioral state indicated by color bars below surf plot. (*D*) The mean maximal γ amplitude for the first hour, normalized to NREM γ power, error bars show SEM (*t* test, **P* < 0.05). *Left* panel shows adult *Lynx1*$^{-/-}$ mice following MD (red, *n* = 10) or no MD (gray, *n* = 8), *Right* panel shows adult DR mice following MD (black, *n* = 5) or no MD (white, *n* = 4). (*E*) Power for the first 2 h of recording comparing representative juvenile *GAD65*$^{-/-}$ mice following MD treated with either saline (black) or diazepam (purple). (*F*) Mean maximal γ power amplitude in *GAD65*$^{-/-}$ juvenile mice with saline treatment and MD (black, no-fill, *n* = 11), with diazepam treatment and MD (juvenile and adult ages combined, purple, *n* = 15), with diazepam treatment and no MD (purple, striped, *n* = 9) and with diazepam treatment as juveniles and MD as adults (wash, purple, no-fill, *n* = 5). one-way ANOVA with Tukey's Multiple Comparison, **P* < 0.05, ***P* < 0.01.

Previous reports have found that deprivation-induced shifts in PV-cell activity are state dependent (11, 24). Cortical activity patterns vary across brain states, differing most dramatically between "sleep" and wakefulness. As expected, baseline γ-power dropped during NREM sleep and the deprivation-induced γ-signature disappeared (blue segments; Fig. 1*B*). Notably, the peak in γ-power reappeared during REM sleep bouts (orange segments; Figs. 1*B* and 2*B*). State differences in acetylcholine drive slow versus fast oscillatory patterns typically observed in different behavioral states (25). Reactivation of the γ-power peak in REM sleep suggested cholinergic signaling may be involved. To explore this hypothesis, we tested mice lacking Lynx1, an endogenous prototoxin that normally dampens cortical nicotinic acetylcholine receptor signaling in adulthood (26). In comparison with nondeprived mice, MD yielded a significant rise in γ-power in adult *Lynx1*$^{-/-}$ animals (mean maximum γ-power no MD = 0.151 ± 0.019, 8 mice; MD = 0.256 ± 0.033, 10 mice; Fig. 2 *C* and *D* and *SI Appendix*, Fig. S2*A*). As in the young WT mice, this γ-power rise was state dependent and reactivated during REM sleep (orange segments; Fig. 2*C*).

Rapid γ-Signature Is Robustly Associated with CP State. Both the absence of MD-induced γ-power in adult WT mice and its presence in adult *Lynx1*$^{-/-}$ animals, which display extended sensory CPs (27, 28), suggest that rapid cortical plastic events are an indicator of open CP state. Therefore, we systematically investigated this relationship across other conditions that shift developmental timing. First, rearing pups in total darkness (DR) from birth delays both the maturation of inhibitory circuits in V1 and CP onset (29). We exposed adult DR mice to light for one day in order to trigger the opening of the CP for ocular dominance. Following MD, these adult mice exhibited a significant rise in γ-power when compared with unsutured DR mice (mean maximum γ-power no MD = 0.057 ± 0.010, 4 mice; MD = 0.162 ± 0.037, 5 mice; Fig. 2*D* and *SI Appendix*, Fig. S2*B*).

Failure to open the CP in DR mice is due to immature cortical inhibition (30), which may also be inadequate to support γ-power. To directly address this hypothesis, we tested mice lacking GAD65. These animals have constitutively low levels of evoked GABA release preventing CP opening, which can be rescued by boosting GABA function at any age (13). MD failed to induce a γ-peak even in young animals (Fig. 2*E* and *SI Appendix*, Fig. S2*C*). However, diazepam treatment for 3 d restored the MD γ-peak over V1 in *GAD65*$^{-/-}$ mice regardless of age (*SI Appendix*, Fig. S2*D*). Diazepam treatment alone without MD did not trigger a rise in γ-power (mean maximum γ-power, saline + MD = 0.074 ± 0.024, 11 mice; diazepam + MD = 0.238 ± 0.0.47, 15 mice; diazepam no MD = 0.084 ± 0.044, 9 mice; Fig. 2*F*). In turn, once a CP was induced by prior diazepam treatment as juveniles then allowed to close (13), MD in adult *GAD65*$^{-/-}$ mice no longer induced a peak in γ-power (mean maximum γ-power = 0.052 ± 0.016, 5 mice; Fig. 2*F*, hollow purple bar).

Rapid TC Synapse Loss onto PV-Cells Heralds CP Plasticity. To examine the synaptic response to this rapid change in oscillatory activity in V1, we optimized a brain slice preparation preserving the TC projection from Lateral Geniculate Nucleus (LGN) to binocular V1 (22). An oblique slice angle was optimized by

age to capture the circuitous fiber trajectory of TC axons both before (P16-18) and during (P24-27) the classical CP (Fig. 3*A*). Connectivity was confirmed by voltage-sensitive dye imaging in response to electrical stimulation of the LGN (Fig. 3*B*). Anatomical boundaries within V1 were established by light exposure to the ipsilateral eye prior to TC slice preparation of Fos-GFP mice: binocular V1 extended laterally (~0.5 mm) from the narrowing white matter tract and contained significantly more cells activated by input from the ipsilateral eye than in neighboring monocular V1 or V2 (Fig. 3*C*). Finally, separate tracer injection into the right and left eyes defined the contralateral and ipsilateral regions within the LGN (Fig. 3 *D*, *Right*). Minimal stimulus currents applied through a pipette placed onto the ipsilateral LGN patch to elicit a V1 response were significantly lower than those for fibers exiting the LGN (Fig. 3 *D*, *Left*), reflecting lower somatic vs. axonal action potential threshold (31, 32).

Minimal stimulus current-evoked TC input drove sharp AMPA-mediated excitatory postsynaptic currents (EPSCs) in layer IV cells of binocular V1 already before the CP (Fig. 4 *A* and *B*). Onset delay (< 9 ms) and jitter (< 0.5 ms) in both PV-GFP and non-PV cells indicated a monosynaptic response (Fig. 4*C*). Notably, EPSC size onto PV-cells was stronger, faster and more precise than that onto neighboring pyramidal cells, as also observed for TC input bias in somatosensory and auditory cortices (28, 33). Threefold larger single-fiber EPSCs were accompanied by a lower paired pulse ratio (PPR), indicating a higher TC release probability onto PV-cells than onto non-PV cells (Figs. 4 *A* and *B* and 5*A*). The shorter onset and faster decay kinetics in PV-cells (Fig. 4*C*) was further consistent with their differential expression of AMPA receptor subunits (34). Importantly, synapse strength and release probability were already fully mature before CP onset (P16-18) similar to the peak of the CP (P24-27), indicating that the TC-to-PV synapse is already stable over this developmental transition (Fig. 4*B*).

We then probed TC connection strength following MD under various conditions. Strikingly, EPSC amplitude onto PV-cells was reduced by nearly half as early as 2 h after MD (Fig. 4*D*). Unlike the transient γ-peak, TC-EPSCs onto PV-cells remained weak through 3 to 4 d of MD (Fig. 4*E*; short-term MD), at which point TC synapse structure (4), dendritic spines (5), and visual response (8) are fully impacted. Consistent with a presynaptic locus, the PPR onto PV-cells was nearly doubled by short-term MD (Fig. 5 *A* and *B*). In the presence of TTX, miniature EPSC (mEPSC) revealed a large decrease in both frequency and amplitude of events onto PV-cells after short-term MD. Surprisingly, TC input onto nearby pyramidal cells was unaltered by short-term MD (Fig. 4*E*) despite a modest decrease in mEPSC amplitude (*SI Appendix*, Fig. S3). As expected for the pivotal role of PV-cells in CP plasticity (9), this TC synapse was only altered when the animal was in a plastic state. Short-term MD neither before CP onset (P16-8) nor in *GAD65*$^{-/-}$ mice during the typical CP (P24-28) weakened TC-to-PV synapse strength (Fig. 4*E*).

Finally, we examined structural changes at the synaptic level. Using vGluT2 to identify TC terminals (35), we compared synaptic puncta onto PV-cell bodies in control animals and after MD (Fig. 5 *C* and *D*). After 3 d of eyelid closure, there was a significant decrease in bouton size but not number surrounding PV-cells in layer IV (Fig. 5*D*). One additional day of MD reduced their number (Fig. 5*E*), reflecting synapse elimination leaving behind only the larger boutons. Thus, the earliest plastic events following sensory deprivation in V1 start with an immediate loss of functional TC input onto PV-cells, consistent with rapid changes in EEG γ-power, followed by presynaptic TC-to-PV synapse shrinkage and pruning several days later. It is likely that these rapid TC-to-PV

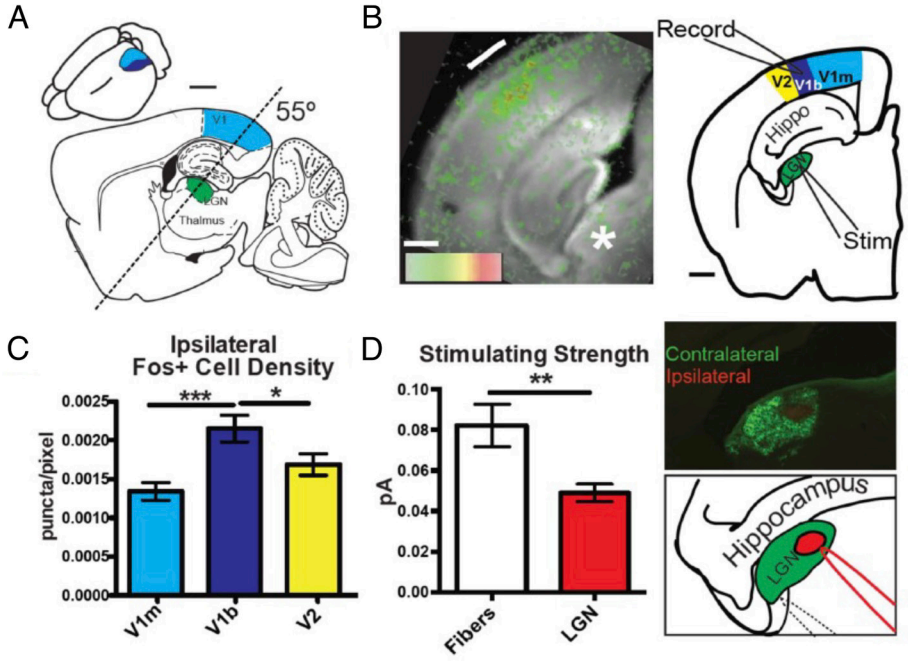

Fig. 3. Validation of the thalamocortical slice. (*A*) Diagram locating LGN and V1, approximately 2 mm lateral of midline, demonstrating the plane of TC slice (dashed line). Inset shows approximate location of monocular V1 (light blue) and binocular V1 (dark blue) in the 3D mouse brain. (Scale bar 500 μm.) (*B, Left*) Individual frame from voltage-sensitive dye recording 8 ms after electric stimulation to the LGN showing strong layer IV activation. (*B, Right*) Diagram of TC slice indicating location of stimulating electrode (Stim) in the thalamus and recording location in the binocular zone of the primary visual cortex (V1b). (Scale bar 500 μm.) (*C*) Quantification of Fos staining in the visual cortex after light stimulus to the ipsilateral eye (n = 9; one-way ANOVA, *P < 0.05, ***P < 0.001). (*D, Upper Right*) Cholera toxin eye injections showing terminals in LGN and separation of ipsilateral and contralateral zones within the TC slice. (*D, Bottom Right*) Diagram of stimulation electrode placement in TC LGN (solid red line) or in fiber tract (dotted line). (*D, Left*) Quantification of initial experiments stimulating either fiber tract or LGN needed to elicit single fiber EPSC. Lines at ± SEM (fiber tract n = 53, LGN n = 40; P < 0.05, Mann–Whitney test).

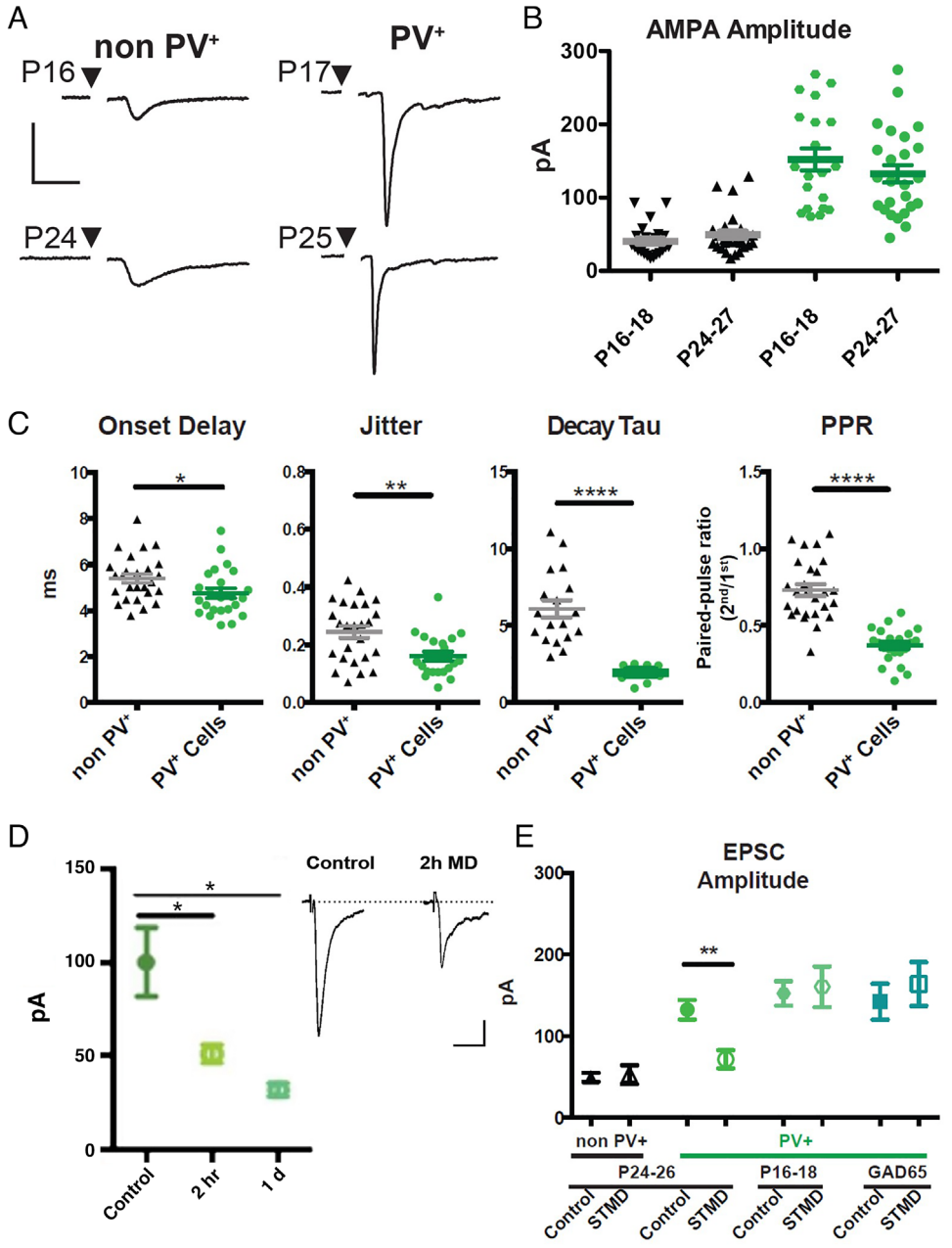

Fig. 4. Thalamocortical input onto PV cells is stronger and more plastic. (*A*) Example traces of AMPA mediated single fiber TC EPSCs onto non-PV cells and PV cells before and during the critical period. (Scale bar 50 pA, 10 ms.) (*B*) Quantification of single fiber TC inputs onto non-PV cells (black) and PV cells (green) before (P16-18) and during (P24-27) the critical period. (*C*) Thalamocortical synapse onto PV+ cells has a higher release probability as indicated by smaller paired pulse ratio, in addition to a quicker onset, less jitter, and faster decay constant than non-PV$^+$ cells. (non-PV$^+$ n = 30, PV$^+$ n = 26). (*D, Right*) Example traces of PV$^+$ cells in control and after 2 h of MD (Scale bar, 20 pA, 10 ms) (*D, Left*) 2 h and 24 h of MD equally decreases the TC input onto PV+ cells. (control *n* = 8, 2 h *n* = 20, 1 d *n* = 7). (*E*) STMD shifts TC EPSCs onto PV+ cells during the critical period but not before the critical period begins nor in animals with reduced GABA signaling (non-PV Control *n* = 30, non-PV STMD *n* = 12, PV+ Control *n* = 24, PV+ STMD *n* = 14; P16-18 Control *n* = 22. P16-18 STMD *n* = 7; GAD65 KO Control *n* = 5. GAD65 KO STMD *n* = 5). Values are mean ± SEM. one-way ANOVA **P* < 0.05, ***P* < 0.01, ****P* < 0.001.

events herald later ocular dominance plasticity and acuity loss as MD proceeds, as all of these events were found to be sensitive to microglial inhibitors [*SI Appendix*, Fig. S4; (36)].

Mathematical Model of Deprivation-Induced Intrinsic Interneuron Network γ-Rhythm (ING). We constructed a biophysical model of thalamic input into layer IV cortical circuits during early developmental periods (pre-CP and CP) (Fig. 6*A*). The model consists of TC-cells, cortical fast-spiking PV-cells and pyramidal cells with 40 neurons of each type. In the pre-CP, all intracortical connections are very weak (silent synapses) representing the unstructured and weak network conditions assumed to be present during early developmental periods. In the pre-CP, PV-cells are connected all-to-all via weak $GABA_A$ synapses.

We assume two populations of PV-cells: one receiving TC input relayed from the right eye and the other receiving TC input originating from the left eye (Fig. 6*A*). Each TC cell in a population connects with all PV-cells in their respective target population. Thus, each PV-cell receives 20 TC inputs. The strong topographic organization present in the early TC system (37–39), the initially sparse innervation of the cortex by the thalamus (40) and the abundance of silent synapses in early development (41) are modeled by each TC-cell connecting strongly to one pyramidal cell and one PV-cell; but otherwise, TC connections are very weak

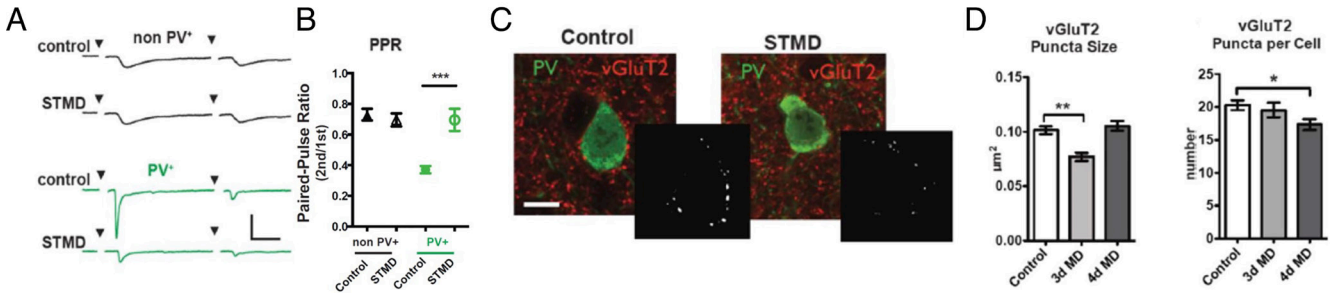

Fig. 5. Presynaptic thalamocortical changes after short-term MD. (*A*) Example traces from control mice and STMD mice of single fiber TC input onto non-PV (black) and PV+ (green) cells. (Scale bar 50 pA, 10 ms.) (*B*) Decrease in PPR suggests changes in release probability after STMD in the PV+ cell (Values are mean ± SEM. non-PV Control $n = 30$, non-PV STMD $n = 12$, PV+ Control $n = 24$, PV+ STMD $n = 14$). (*C*) PV and VGluT2 staining of PV^+ cells in control and MD animals after 3-d MD. *Inset* images after establishing the ROI and thresholding. (Scale bar 20 μm.) (*D*) 3 d of MD shows a decrease in puncta size while after 4 d there is a decrease in number of puncta (*E*) ($n = 4$ animals per group, 10 cells for each area per animal. one-way ANOVA with Tukey's Multiple Comparison $^*P < 0.05$. $^{**}P < 0.01$).

(silent) (Fig. 6*A*). In fact, we find that this pre-CP connection scheme is necessary to prevent plasticity during the pre-CP (see *SI Appendix* section entitled "Relaxation of model assumptions") and enables a simple and principled representation of early thalamic input to the cortex. Although, pyramidal cells receive input from the TC cells of both TC populations, since only one TC-to-PYR connection is strong enough to elicit spiking for each layer IV PYR (throughout all simulations), the TC-to-PYR connections are effectively monocular.

The transition from the pre-CP to the CP state is achieved by adding electrical connections between PV-cells and strengthening PV-to-PV inhibition, as suggested by experimental work (23, 42). At CP onset, PV-cells connect electrically with all other PV-cells of their own population (those receiving input derived from the right or left eye, respectively), and $GABA_A$ connections between all PV-cells are strengthened. Assuming there is greater competition between PV populations than within populations, $GABA_A$ conductance is stronger for inhibitory connections between versus within populations (see *SI Appendix* section entitled Relaxation of model assumptions for simulations without this assumption).

We model MD by stopping the spiking of half of the TC-cells (those receiving input from the deprived eye), which effectively stops the spiking of all PV and pyramidal cells to which those TC-cells project strongly (Fig. 6*B*). We refer to the population of PV-cells deprived of TC input as PV_{MD} cells and to the population of PV-cells receiving TC input from the open eye as PVo cells (Fig. 6*A*). We model the local field potential (LFP) as the sum of inhibitory currents onto pyramidal cells (43–45) (*SI Appendix*, Methods).

MD Induces ING in the PVo Population. A finely tuned γ-oscillation around 40 Hz emerges in the model LFP immediately upon loss of input to half of the TC-cells during the CP (MD_{early} condition) but fails to do so without MD (Fig. 6*C*), consistent with our experimental results (Figs. 1 *B* and *C* and 2*A*). As observed in vivo (Figs. 1*B* and 2*C*), the γ-oscillation induced by MD in the model persists for a discrete period of time, gradually increasing in frequency before finally disappearing (MD_{late} condition) (Fig. 6*C*). Our computational model thus reproduces the major EEG features of the acute yet transient rise in γ-power following MD during the CP in mice.

The model further allows us to observe the spiking and network dynamics of the thalamic and cortical neurons to determine causative factors underlying the MD-induced γ-rhythm as well as network changes brought about by the γ-rhythm. MD is modeled

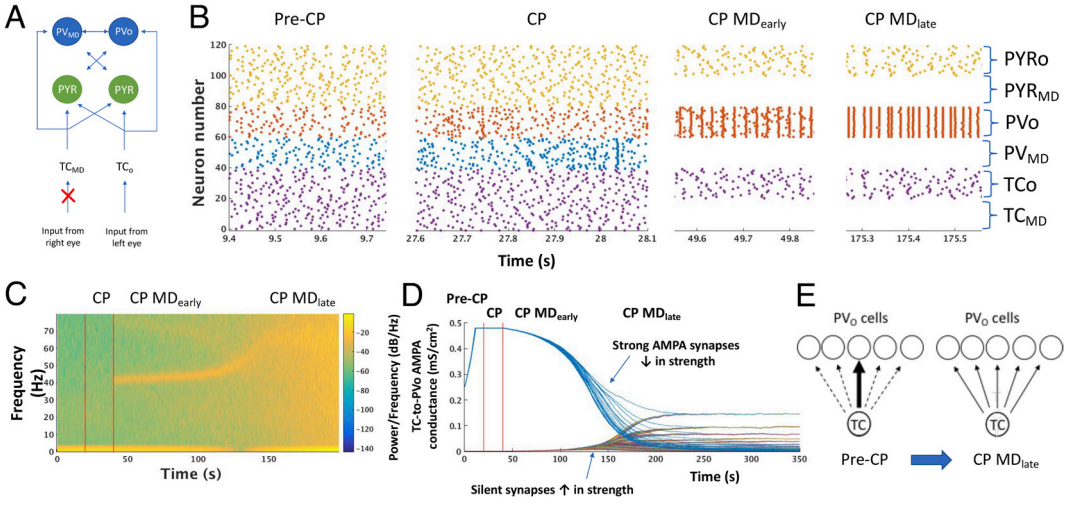

Fig. 6. Computational model of MD during the CP. (*A*) Schematic diagram of the model thalamocortical network. TC_{MD}/TC_O refers to the TC population receiving input from the monocularly deprived and open eye, respectively. PYR_o / PYR_{MD} and PV_o / PV_{MD} refer to the populations of pyramidal or PV-cells receiving strong input from TC_O and TC_{MD}, respectively. (*B*) Representative raster plots of all neurons in the thalamocortical network during the pre-CP, CP and CP MD_{early} and CP MD_{late} states. (*C*) Spectrogram of model LFP as the model transitions from pre-CP to CP (first vertical red line) then to CP+MD (second vertical red line). (*D*) Evolution of all model TC-to-PV_O synaptic AMPA conductances through the pre-CP, CP and CP+MD states (red vertical lines demarcate the boundaries between states). Each curve shows the AMPA conductance of one TC-to-PV_O synapse over time. (*E*) Schematic of the redistribution of TC-to-PV_O connectivity induced by CP MD. Arrow thickness represents connection strength.

by stopping the spiking of half of the TC neurons (TC_{MD} neurons) as seen by lack of activity in neurons 1 to 20 in the raster plot during CP MD (Fig. 6*B*). As a consequence of loss of TC_{MD} input, both PV_{MD} neurons and pyramidal cells receiving strong input from TC_{MD} stop spiking. In contrast, the spiking of the PVo neurons, which faithfully followed strong TCo input during the pre-CP, begin to spike synchronously at intervals in the γ-frequency range following MD (Fig. 6*B*). This spontaneously formed interneuron ensemble of PVo cells is an expression of a well-characterized rhythmic dynamic in neuronal systems termed an interneuron γ (ING) rhythm (19, 20). We note that the formation of ING occurs immediately upon cessation of PV spiking from the PV_{MD} population deprived of TC input (Fig. 6 *B* and *C*).

Notably, we do not see an acute rise in γ-rhythms as the model transitions from pre-CP into the CP without MD (Fig. 6*C*), again consistent with our experimental finding (Fig. 1 *B* and *C*). This lack of an abrupt onset of γ-rhythm following CP opening alone (i.e., addition of electrical connections and strengthened inhibition between PV-cells) is consistent with known mechanisms of ING, which require sufficient interneuron excitation. The latter condition is provided by MD: release of inhibition from the deprived PV population (PV_{MD} cells) allows the PV cells receiving input from the open eye (PVo cells) sufficient excitation to form ING. Thus, the MD-induced formation of ING during the CP is due to a dramatic and sudden imbalance of excitation to the two interconnected interneuron populations, leaving the PVo population in a high excitation state and thus able to form ING.

ING Alters TC-to-PV Spike Timing and Enables Rapid Plasticity. The formation of an ING ensemble has immediate consequences regarding network plasticity. Since the spike timing of the PVo cells is no longer driven exclusively by the TC input, but additionally has its own intrinsic ensemble dynamics, spike timing between TC-cells and PVo cells is no longer solely sequentially pre–post as occurs in the pre-CP (*SI Appendix*, Fig. S5*A*). The consequence of this altered spike timing is a rapid and progressive depression of AMPA connection strength in the strong TC-to-PVo connections (Fig. 6*D* and *SI Appendix*, Fig. S5*B*). This is consistent with the finding of decreased TC-to-PV AMPA responses following MD during the CP in mice (Fig. 4 *D* and *E*). In contrast, TC-to-PV_{MD} connections remain unchanged since no spike-timing-dependent plasticity occurs in the absence of spiking (see "Synaptic Plasticity Rules" in *SI Appendix*, *Methods*). The TC input to the pyramidal cells also remains unchanged due to the unaltered spike timing between TC cells and pyramidal cells following MD (*SI Appendix*, Fig. S5 *A* and *C*), consistent with our experimental observations of TC-to-PV cell-specific plasticity (Fig. 4*E*).

In contrast, modeling MD before the CP does not yield any significant changes in oscillatory power (*SI Appendix*, Fig. S5*D*) or any plastic changes (*SI Appendix*, Fig. S5*E*): due to lack of electrical connections in the pre-CP, the ING rhythm does not emerge and pre–post spiking from TC-to-PV cells remains unaltered – again consistent with the experimental results showing lack of plasticity before the CP (Fig. 4*E*). These results point to the developmental importance of gap junctions between PV interneurons in regulating behaviorally relevant plasticity during the CP.

The rapidity of the ING-induced plastic changes occurs due to the ING-imposed ~25 ms PVo interspike interval (Fig. 6*B*, see CP MD_{early}), which ensures significant plasticity in TC-to-PVo connections (either LTD or LTP) on every γ-cycle (*SI Appendix*, Fig. S5*F*, see Synaptic Plasticity Rules section in *Methods*). This accounts for the rapid evolution of TC-to-PV plastic changes observed both in the model and in vivo. We note that plasticity in the model evolves more rapidly than in vivo (100 s of model time corresponds to approximately 2 h of in vivo time) due to the instantaneous nature of the plastic changes in the model. In contrast, in vivo plastic changes are not instantaneous but rather depend on intracellular signaling pathways as well as periods of sleep (11, 46). In a subsequent section below, we examine why LTD predominates over LTP in altering the strong TC-to-PVo synapses. Overall, our modeling suggests that the MD-induced γ-rhythm is a signature of ING, an autonomous cortical dynamic independent of specific thalamic input. The autonomous nature of ING alters TC-to-PV spike timing, resulting in an observed decrease in TC-to-PV connectivity strength.

Rising γ-Frequency and Eventual Disappearance Reflects Strengthening of Silent Synapses. Our experimental recordings show the frequency of the γ-rhythm increasing over several hours following MD before finally disappearing (Figs. 1*B* and 2*C*). The model reproduces these findings (Fig. 6*C*) and reveals that these features of the γ-frequency signature are due to increasing the strength of previously silent TC-to-PV synapses, which follow the decrease in previously strong TC-to-PV synapses (Fig. 6*D*). Decreasing the conductance of the strong TC-to-PV synapses is essential to unmask the contribution of silent TC-to-PV synapses due to a limit built into the model on the overall amount of excitation a PV-cell can receive, a principle related to homeostatic synaptic scaling of excitatory synapses (47, 48). During the pre-CP, TC-to-PV synapses with the greatest AMPA conductances dominate the overall input to any particular PV-cell, while the remainder of TC-to-PV synapses remain silent (Fig. 6*D*). Standard Hebbian plasticity rules at the TC-to-PV synapse maintain the dominance of this strong connection, not allowing the silent TC-to-PV synapses to emerge. Decreasing the strength of the strong TC-to-PV synapse in response to ING opens a window of opportunity for the silent synapses to increase in strength (Fig. 6*D*).

Both the rising γ-frequency and its eventual disappearance are signatures of TC-to-PV conductance increases in previously silent synapses. Since the overwhelming majority of TC-to-PVo synapses (19/20 synapses to each PVo cell in our model) are silent at the start of the CP, the overall effect of weakening previously strong synapses to unmask previously silent synapses is to increase excitation onto the PV-cells. In turn, as PV-cell excitation increases, the γ-frequency of the ING increases (20). Thus, our model suggests that the experimentally observed time period over which MD-induced γ-oscillations are increasing in frequency corresponds to when silent TC-to-PV synapses are becoming active. Eventually, the majority of TC-to-PV synapses gradually become similar in strength. This transforms the spiking of PV-cells from a network in which one PV-cell responds only to the input of one, strongly connected TC-cell to a network in which the total TC population guides the PV network spiking activity (Fig. 6*E* and *SI Appendix*, Fig. S6).

As this transition takes place, the finely tuned γ-rhythm fades out and is replaced by a broadband increase in power (Fig. 6*C* MD_{late}). This is due to the overall increase in TC population AMPA to the PV-cells, which drives them to spike in response to TC population activity: thus, ING is replaced by PV-cells being synchronized to TC population input, which is nonrhythmic and generally at a faster rate than ING (Fig. 6*B*, CP MDlate) and appears in the model LFP as broadband activity. Thus, our model predicts that the disappearance of narrow-band γ-rhythm after MD corresponds to the time when TC-to-PV synapses have strengthened enough to be patterned by TC population activity.

Complementary changes in TC synapse strength in response to ING reflect the nonsymmetrical spike-timing-dependent

plasticity rule of PV-cells in which LTD has a longer time constant of decay than LTP (*SI Appendix*, Fig. S5*F* and *Methods*) as well as the upper and lower limits on AMPA conductance and the way Hebbian rules act around these limits. Specifically, silent synapses are close to the lower limit of AMPA conductance (near gAMPA = 0), which favors LTP as maximal LTD cannot occur if that moves gAMPA below the lower limit; while, LTP can always be maximally instantiated near the lower conductance limit. Thus, if spike-timing-dependent plasticity is allowed to occur, and pre–post spikes are randomly aligned as occurs with TC-to-PV synapses during ING, silent synapses will be strengthened. The opposite phenomenon occurs for the strong TC-to-PV synapses, which are near the upper limit of AMPA conductance favoring LTD over LTP. Once away from the upper and lower limits of AMPA conductance, synapses compete until a semistable equilibrium is reached in which all TC-to-PV synapses become more homogeneous in strength (Fig. 6*D*).

These results suggest that the temporal dynamics of the EEG γ-rhythm following MD are signatures of TC-to-PV circuit rewiring. The network evolves from a TC-to-PV network in which each PV cell is predominately driven by one strong TC input (*SI Appendix*, Figs. S5*A* and S6*A*) to a network that uses the collective TC input to drive a strong, synchronized PV output (*SI Appendix*, Fig. S5*A* and S6*B*). The PV output is both weak and narrowly defined in scope during the pre-CP: one PV-cell responds primarily to one TC-cell spike. In contrast, after CP rewiring the PV output is strong (an ensemble of PV-cells transmits synchronously) (*SI Appendix*, Fig. S6*C*) and broader in scope (PV-cells respond to many combinations of TC input) (*SI Appendix*, Fig. S6*B*).

The CP rewiring after MD also improves sensitivity of PV-cells to TC input: namely, input that previously would not have caused PV-cell spiking now reliably produces robust PV-cell output (*SI Appendix*, Fig. S6 *A* and *B*). Gap junctions between PV-cells underlie their increased sensitivity to TC input since electrical coupling between cells increases their excitation and effectively lowers their spiking threshold (23, 49). Relatively homogeneous TC-to-PV synapses, along with gap junctions, contribute to all PV-cells spiking synchronously in response to TC input, since each PV-cell is receiving approximately the same amount of depolarizing input as all others. Increased sensitivity in turn enhances the fidelity of TC transmission to the cortex by post-MD network modifications: the PV population more faithfully encodes the collective output of the TC population (*SI Appendix*, Fig. S6*B*).

Overall, our results suggest the post-MD γ-signature serves as a functional read-out of TC-to-PV connections transitioning from a network producing weak feedforward inhibition from single TC-cells to a network that sensitively responds to TC population statistics, amplifying this signal, and thus sending coordinated and powerful inhibition within cortical circuits.

Compensatory Mechanisms Limit the Rise in Broadband γ-Power. Some form of homeostatic renormalization of E-I balance is likely to take place after the restructuring of TC-to-PV synapses, as overall excitation to PV-cells has grown considerably over the course of MD (*SI Appendix*, Fig. S6*C*). Common mechanisms for decreasing PV excitability include a compensatory, uniform decrease in all TC-to-PV synapses, decreased PV-to-PV electrical connectivity, increased PV-to-PV GABAergic inhibition or regulation of specific intrinsic PV membrane currents leading to additional membrane hyperpolarization (e.g., increasing Cl^- leak).

To examine the effect of decreasing PV excitability, we lowered the maximal gap junctional conductance between PV-cells after bouts of simulated sleep (simulated by reducing cortical spiking), hypothesizing that repeated activity bursts during slow-wave sleep may decrease coupling between PV cells as they do between cells in the thalamic reticular nucleus (50). These simulations reproduced the slight drops in γ-frequency after bouts of non-REM sleep seen in our mouse experiments (Fig. 1*B*) and mitigated the degree of broadband LFP activity at MD_{late} stages (Fig. 7*A*). Yet, the decrease in PV-cell activity did not affect the overall progression of TC-to-PVo synapses toward homogeneity (Fig. 7*B*), regardless of a lack of plasticity during sleep due to the absence of spiking. Toward the end of the simulation, the almost perfect synchrony between PV-cells which occurs when gap junctions remain strong (Fig. 6*B*) was replaced by a jittered synchrony when gap junctions were weakened (Fig. 7*C*), which ultimately decreases broadband γ-power (Fig. 7*A*), as observed in vivo (Fig. 1*B*). As such, we expect that some sort of compensatory mechanism for PV overexcitability accounts for these changes in vivo.

Competitive ING Dynamics Arise between PV Populations During Normal CP Experience. Modeling the CP without MD elicits a slow onset of ING-like dynamics in both populations of PV cells expressed at alternate times (*SI Appendix*, Fig. S7*A*). The CP is modeled by adding gap junctions between a population of PV-cells and increasing the $GABA_A$ conductance between PV neurons. Without MD, the TC inputs from the two thalamic regions are approximately equal (same mean spiking rate) and there is no immediate emergence of γ-activity in our model LFP (*SI Appendix*, Fig. S7*B*), rather γ-activity slowly builds up over

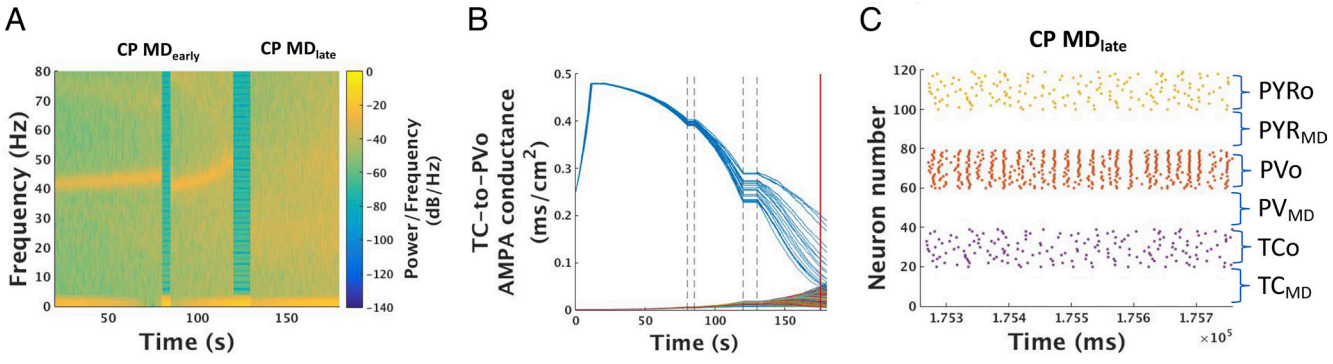

Fig. 7. Network dynamics of CP+MD with homeostasis. (*A*) Spectrogram of model LFP during the CP+MD state with interspersed periods of artificially simulated sleep (see *SI Appendix, Methods*) at 80 to 85 s and 120 to 130 s. Gap junction conductance was lowered after each period of sleep in order to compensate for PV-cell overexcitability. (*B*) Evolution of all model TC-to-PV_O synaptic AMPA conductances during the pre-CP (0 - 20 s) as well as during the same time period as shown in (*A*). Dashed vertical lines demarcate periods of sleep. (*C*) Raster plot of all model neurons as TC-to-PV_O synaptic conductances approach a more homogeneous state during CP MD_{late} at the timepoint indicated by the red vertical line in (*B*).

the course of the CP. Early in the CP, PV-cells largely spike in response to the strong TC input, while only occasionally spiking without it (*SI Appendix*, Fig. S5*A*). Moreover, when spiking independently of TC input, the PV spiking is coordinated with that of others such that synchronous spiking occurs among many of the PV-cells in the population (*SI Appendix*, Fig. S5*A*). This may occur as a single bout or as several bouts of synchrony occurring at γ-frequency (SI Appendix, Figs. S5*A* and S7*A*). This PV-cell dynamic is a manifestation of ING, although the ING is not as persistent or robust as in the case when MD occurs during the CP (Fig. 6*B*). ING occurs transiently in a population of PV-cells due to fluctuations in excitability: if one PV population receives more TC excitation and/or less PV inhibition from the other PV group, the more excited PV-cells can form ING.

Thus, our model suggests that ING expression during normal CP experience is sporadic and brief, resulting from competition between PV-cell populations. Each bout of ING has the potential to rewire the TC-to-PV synapses in a similar manner to the rewiring that occurs during MD. The rewiring process is longer for normal CP experience than with MD due to the noncontinuous, short bouts of ING (compare Fig. 6 *C* and *D* and *SI Appendix*, Fig. S5 *B* for CP with MD and *SI Appendix*, Fig. S7 *B* and *C* for CP without MD). Eventually, TC-to-PV synaptic connections even without MD lead to a γ-oscillation that increases in power and frequency (*SI Appendix*, Fig. S7*B*). This result is consistent with the gradual emergence of γ-power through the CP (21). When the silent TC-to-PV synapses have strengthened sufficiently to control the spiking dynamics of the PV population to which it connects, the ING disappears and a broadband γ-power emerges (*SI Appendix*, Fig. S7*B*).

Thus, we find that the network dynamics that evolve as they naturally pass through the CP are similar to those that evolve with MD, though not as abrupt nor necessarily restricted to one population of PV-cells. The statistics of the environment determine the outcome of the competition between groups: the PV population that receives more TC excitation undergoes more bouts of ING and thus faster TC-to-PV re-wiring, and significantly imbalanced input can lead to inhibition of TC-to-PV rewiring in the population receiving less input. These dynamics thus represent a natural coding mechanism for wiring of TC circuits based on the statistics of the environment.

Discussion

A canonical model of critical period plasticity is the gradual loss of connectivity and visual acuity through an eye deprived of vision early in life (8). Our experimental results here reveal that the initial plastic processes occur at thalamic synapses onto inhibitory PV-cells in cortical layer IV. Within hours of MD, TC input onto PV-cells drops dramatically but only when the CP is open. An immediate rise in narrowband γ-oscillations upon eyelid closure appears to drive this change in TC-to-PV synaptic strength. The fleeting γ-rhythm increases in frequency and eventually fades out over several hours, while the decrease in TC-to-PV presynaptic input persists by anatomical pruning over several days (when visual acuity is finally impacted). Computational modeling of these biological events offers a functional relationship between the initial γ-oscillation and resultant plastic changes at TC-to-PV synapses, reinforcing the pivotal role of inhibitory networks as triggers of the developmental CP (9).

Our model reproduces the emergence and evolution of the γ-oscillation after MD and suggests CP physiology is primed for the establishment of ING (interneuron γ) dynamics between cortical PV-cells. The expression of transient γ-rhythms requires sensory input, as evidenced by their absence in total darkness (Figs. 1*D* and 2*A*). ING results from elevated PV-cell excitation, with MD being an extreme form of PV cell excitation due to imbalanced thalamic input. As an autonomous cortical dynamic, ING dissociates TC and PV spiking, which leads to weakening of initially strong TC-to-PV synapses by standard STDP rules. This in turn allows previously silent TC-to-PV synapses to strengthen in our model. Molecular homeostatic factors, such as NARP (48) and SynCAM1 (51), may regulate this maturation of TC input onto PV-cells in V1. Interestingly, the upward drift of γ-oscillation frequency is a signature of the emergent boosting of silent synapses. Fade-out of the rhythm occurs once the population TC-to-PV synaptic strength has increased sufficiently to override ING dynamics.

Our model predicts that ING is the forerunner to synaptic changes at TC-to-PV circuits and as such if ING does not appear, neither will the synaptic changes. Before the CP, inhibition between PV-cells is immature (42) as are their electrical connections (23)—inadequate network conditions for ING to form. Well-developed PV-to-PV synapses enable competing PV groups to sensitively detect imbalances in thalamic input. The PV population that receives more excitation relative to its competing PV population reliably forms ING, rendering itself susceptible to TC-to-PV synaptic weight changes. Conversely, the well-known condensation of perineuronal nets (PNNs) around mature PV-cells at CP closure sufficiently diminishes their response to glutamatergic transmission, and thus their overall excitability (52), so that ING can no longer form. In fact, PNN removal by chondroitinase ABC-treatment unmasks a rapid rise in narrowband, ING-like γ-oscillation following MD in adult rats (53), supporting CP reopening. Thus, MD-induced ING is a specific PV network dynamic reflecting conditions that underlie the plastic state.

Interestingly, our simulations indicate that TC to PV circuit reorganization is largely complete with the emergence of broadband γ power in the LFP, a sign that ING has been replaced by PV neurons responding more readily to population-level TC input. Consistent with this, Faini et al. (52) found that dissolution of PNNs leads to a slow broadband increase in baseline and visually evoked γ-power 2 to 3 d later. They additionally found increased TC input to layer IV PV-cells after PNN dissolution, consistent with our model prediction of increasing TC-to-PV synaptic strength during juvenile CPs of development. However, unlike the juvenile state in which the majority of TC-to-PV synapses are initially silent, TC-to-PV synaptic strength should be more homogeneous in the adult. Thus, the rise in TC-to-PV synaptic strength is more detectable during a reopened adult CP state, once physiological conditions necessary for ING formation are reestablished.

Our study clarifies the earliest sequence of changes in V1 following MD. How the rapid TC-to-PV plastic changes in layer IV within 2 h of deprivation contribute to later changes across cortical layers is of interest. We find PV-cell activity in layer IV increases after MD specifically among those PV cells receiving input from the open eye. Considering that these interneurons connect to layer II/III interneurons (54), supra-granular PV-cell response to the open eye is expected to decrease at first and continue to evolve days after MD (10). In fact, changes in layer II/III PV-cells are detectable after 6 h of MD also in kittens (11) and initially shift their responsiveness in favor of the closed eye (10). Note that calcium imaging in mice had previously suggested that other GABA cells likely shift their responsiveness only days later (55).

Strikingly, the first recorded change in layer II/III following MD is increased coincident spiking (±10 ms) among open eye-responsive pyramidal-PV cell pairs (11). This alteration in spike timing takes

place 1 h after MD, exactly when we found MD-induced γ-rhythms to emerge. An increase in nearly coincident spike timing between pyramidal-PV cell pairs is precisely what would be expected from layer IV ING that synchronously releases them from inhibition for only a very short period of time at the end of each γ-cycle (19, 20). Such an increase in nearly coincident spiking between pyramidal-PV cell pairs is also expected when mesencephalic stimulation successfully drives γ-rhythms in adult cat V1 to enable plasticity of receptive field properties (56).

Shifts in neuromodulatory activity over the first several hours of MD may contribute to the transient nature of the observed rise in γ-power. The presence of a γ-peak in both wake and desynchronized (REM) sleep, but not in NREM sleep, suggests cholinergic signaling may be involved. Visual γ-power can be dramatically increased for several hours by pairing visual stimuli even briefly with cholinergic agonists (57). A similar 'novelty' detection may arise post-MD, with concordant loss of thalamic drive onto PV-cells and increased cholinergic tone creating a cortical state that favors γ-activity. Acetylcholine has long been appreciated to play an important role in regulating CP plasticity (58). During the auditory CP, acetylcholine activates layer I inhibitory interneurons, which in turn inhibit PV-cells from the top down (28). Boosting cholinergic signaling in adult mice either pharmacologically or through genetic deletion of *Lynx1* re-opens CP plasticity across brain regions (27, 28).

One theory of CP timing postulates that inhibition opens windows of plasticity by increasing the signal-to-noise ratio (59), shifting the brain's sensitivity to external stimuli as opposed to internally generated activity. By locally altering signal-to-noise dynamics of a network (60), the γ-rhythm may mediate shifts between external and internal cues. Our modeling supports the notion that a function of the rewired TC-to-PV network in the adult cortex may relate to suppression of noise as a means of increasing fidelity of TC signal transmission when passing sensory input to the cortex. Whereas TC-to-pyramidal cell synapses likely encode the specificity of the input, TC-to-PV connections responding to the population TC input provide background inhibition. This filters out the weaker pyramidal cell activity unrelated to the specific TC input. Our study suggests CP rewiring of TC-to-PV input contributes to the ability to reduce noise, and thus increase gain, in adult circuits.

We also provide an explanation of how more subtle naturalistic experiences early in life can ultimately shape neural circuits during the CP. While a strong, transient γ signature (lasting ~110 s of simulation time) follows strong input imbalance (like MD) in the model, only brief ING (~10s of milliseconds) follows the less dramatic fluctuating thalamic input statistics under normal environmental conditions. Small plastic changes then accrue such that TC-to-PV plastic changes occur predominately in the TC pathways receiving environmentally dominant stimuli. Overall, the EEG γ-signature following MD is a read-out of TC-to-PV connections transitioning from a network that provides weak feedforward inhibition of strong thalamic signals to a network that sensitively responds to TC population input and amplifies this signal, providing coordinated and strong inhibition to local cortical areas.

More broadly, γ-oscillations are associated with cognition and altered in cognitive disorders like autism and schizophrenia (61). Our findings now refine a potential role for these oscillations to specific time windows that enable network plasticity. Our model suggests that the physiological changes supporting ING are necessary for CP opening. Notably, adult rhythms measured once this initial plastic period has passed may fail to detect any consistent relationship to the deficits. For example, inhibiting mediodorsal and midline thalamus in mice during adolescence leads to long-lasting decreased thalamo–prefrontal projection density and later cognitive deficits (62). While γ-rhythms are not altered during task performance in adulthood, their role during the adolescent CP itself remains to be tested. In multimodal, higher order brain regions such as the prefrontal cortex, sequentially disrupted or misaligned CPs from lower order areas may further accumulate (63, 64). Appreciating how γ-oscillations contribute to developmental trajectories of plasticity offers a biomarker for tracking and treating these complex cognitive disorders.

Materials and Methods

Experimental.

Mice. C57Bl/6J, PV-GFP, *GAD65*$^{-/-}$ and *Lynx1*$^{-/-}$ mice were bred in-house and maintained on a 12-h light/dark cycle, with the exception of dark-reared animals. All experimental procedures followed Institutional Animal Care and Use Committee guidelines.

Surgery. For MD, mice were sedated with isoflurane and one eyelid trimmed and sutured shut as previously described (5). For EEG, insulated stainless steel recording electrodes (100 μm diameter, 1 mm exposed tip) were slipped between the skull and cortex with the tip overlying binocular V1 (or S1 as control) and cemented to the skull in a plug at least 4 d prior to MD. EEG recording in a sound-proof box was begun 10 min following recovery from anesthesia for MD. Recordings were high-pass filtered through a preamplifier (Pinnacle Technology 8202-SL), further amplified (Brownlee) and collected using either VitalRecorder (Kissei) or Sirenia Acquisition (Pinnacle Technology).

Slice electrophysiology. Brains were rapidly removed from deeply anesthetized mice into ice-cold choline-based cutting solution and cut at an oblique angle (~55° depending on age) to preserve TC projections to V1, as described previously (22). Slices were incubated in oxygenated ACSF (125 mM NaCl, 25 mM glucose, 25 mM NaHCO3, 2.5 mM KCl, 2 mM CaCl2, 1.25 mM NaH2PO4 and 1 mM MgCl2 (310 to 320 mOsm) for recording at 20 to 22 °C. Projections to V1 were initially confirmed by voltage-sensitive dye imaging (VSDI; 5 μg/mL Di-4-ANEPPS; Invitrogen) using a band-pass-filtered (515 and 535 nm) 150-W halogen lamp on an upright macroscope (Olympus MVX10) mounted with a high-speed CMOS-based camera (MiCam Ultima).

Single cells in binocular V1 were visualized and recorded under infrared-Nomarski DIC optics on an upright microscope (40×; Eclipse FN1, Nikon) using whole-cell patch-clamp techniques. Electrodes (2 to 4 MΩ) were filled with internal solution containing (in mM) 120 Cs-methanesulfonate, 6 CsCl, 2 MgCl2, 0.05 CaCl2, 20 HEPES, 0.02 EGTA, 10 phosphocreatine di(Na) salt, 4 Mg-ATP, 0.4 Na3-GTP, 0.15% biocytin, and 1 lidocaine derivative QX-314 (pH 7.2 with CsOH, 290 to 300 mOsm). Access resistances were maintained < 25 MΩ throughout the experiments. Bipolar glass stimulating electrodes filled with ACSF were placed in the LGN or fiber bundle to stimulate TC input with minimal current in the presence of 10 μM bicuculline.

Immunohistochemistry. Mice were perfused transcardially with paraformaldehyde (4% PFA) and brains removed, postfixed in PFA (1.5 h) and cryoprotected (30% sucrose) before slicing into coronal sections (40 μm) on a cryostat or freezing microtome (Leica). Every fourth section was collected, washed in phosphate-buffered saline (PBS), incubated in blocking solution (0.8% Triton X- 100, 20% BSA in PBS; overnight, 4 °C), then primary antibody (rabbit anti-GFP 1:2,000 (Abcam), rabbit anti-PV 1:1,000 (Swant), guinea pig anti-VGluT2 1:500 (Synaptic Systems) followed by secondary antibody (goat anti-rabbit IgG Alexa 488, goat anti-rabbit IgG Alexa 596, goat anti-guinea pig 564, goat anti mouse 488 or 633 (Invitrogen), diluted at 1:1,000 in PBS-Triton-BSA). PV-cells were imaged on a scanning confocal microscope (Olympus Fluoview FV1000TM) at 100×. The number of VGluT2 immunoreactive puncta surrounding a PV+ cell body was estimated using a custom MatLab script to identify a 1.25-μm ring around each cell. The red VGluT2 channel was thresholded to the median intensity plus 4× the SD, and all puncta within the ring, larger than 3 pixels (0.123 μm), were automatically counted and analyzed.

Computational Methods.

Neurons. Our cortico-thalamic model consists of 120 single compartment neurons with Hodgkin–Huxley-type dynamics for the intrinsic and synaptic currents. The model of cortical layer IV of V1 consists of 40 fast-spiking PV cells and 40

pyramidal cells (PYR cells). Each neuron has spiking currents (fast sodium, fast potassium and leak currents). Model pyramidal cells have an additional M-current to account for the spike-frequency adaptation observed in these cells. The model neurons were derived from (65, 66). Our thalamic model consists of 40 thalamocortical cells (TC cells) and is used solely for the purpose of passing sensory input to the cortex. Thus, TC cells are modeled using only the spiking currents. The TC cells receive independent noisy inputs to mimic fluctuating sensory inputs. Details of the equations and parameters used for each type of model neuron can be found in the *SI Appendix, Methods*.

Networks. Twenty TC cells receive input that is considered to come from the right eye (TC_R) and the other twenty TC cells receive input considered to come from the left eye (TC_L). Thalamic neurons project more strongly to one PYR cell and one PV cell and relatively weakly to all other pyramidal cells and to PV cells of the same PV population (PV cells receive input from either TC_L or TC_R). PV cells that receive input from TC_R connect less strongly to other PV cells that receive input from TC_R and more strongly to PV cells that receive input from TC_L and vice versa for PV cells that receive input from TC_L. This network connectivity scheme is used to model lateral inhibition between different functional units of interneurons. Additionally, gap junctions (when present) are only put between PV cells of the same functional unit (i.e., those receiving input from TC_R or from TC_L).

In the pre-CP, all intracortical connections are weak because we are interested in the early (unspecified) state of the cortex. All inhibitory synapses use $GABA_A$ receptor kinetics and all excitatory synapses use AMPA receptors. Cortical PV cells are connected all-to-all via $GABA_A$ receptors with stronger connections between PV populations than within a population. The critical period is modeled by strengthening all PV-to-PV maximal conductances and adding electrical connections between PV neurons of the same population. Details of the equations and parameters used for the synaptic conductances are in *SI Appendix*.

Detailed methods can be found in *SI Appendix*.

Data, Materials, and Software Availability. Computer simulation data have been deposited in GitHub (https://github.com/mmccart/Quast-et-al-C--code) (67). All study data are included in the article and/or *SI Appendix*.

ACKNOWLEDGMENTS. We thank M. Nakamura, M. Marcotrigiano, E. Centofante, H. Bond for mouse maintenance; H Monyer (Heidelberg) and A Barth (Carnegie Mellon) for original PV-GFP and Fos-GFP breeders, respectively and M. Fagiolini for advice and support. Funded by NSF GRFP (DGE0946799, DGE1144152 to R.K.R), NIH Research Training Program in Sleep, Circadian & Respiratory Neurobiology (5T32HL007901-23 to R.K.R.) and NIMH Silvio Conte Center (1P0MH094271 to N.K. & T.K.H.). This article is dedicated to the memory of Prof. Miles Whittington (d.10/25/2021).

Author affiliations: [a]Department of Molecular Cellular Biology, Center for Brain Science, Harvard University, Cambridge, MA 02138; [b]FM Kirby Neurobiology Center, Boston Children's Hospital, Harvard Medical School, Boston, MA 02115; [c]Department of Mathematics, Boston University, Boston, MA 02215; and [d]International Research Center for Neurointelligence, University of Tokyo Institutes for Advanced Study, Bunkyo-ku, Tokyo 113, Japan

1. D. H. Hubel *et al.*, Plasticity of ocular dominance columns in monkey striate cortex. *Philos. Trans. R. Soci. Lond. B Biol. Sci.* **278**, 377–409 (1977).
2. A. Antonini, M. Fagiolini, M. P. Stryker, Anatomical correlates of functional plasticity in mouse visual cortex. *J. Neurosci.* **19**, 4388–4406 (1999).
3. M. A. Silver, M. P. Stryker, Synaptic density in geniculocortical afferents remains constant after monocular deprivation in the cat. *J. Neurosci.* **19**, 10829–10842 (1999).
4. J. E. Coleman *et al.*, Rapid structural remodeling of thalamocortical synapses parallels experience-dependent functional plasticity in mouse primary visual cortex. *J. Neurosci.* **30**, 9670–9682 (2010).
5. N. Mataga, Y. Mizuguchi, T. K. Hensch, Experience-dependent pruning of dendritic spines in visual cortex by tissue plasminogen activator. *Neuron* **44**, 1031–1041 (2004).
6. S. Oray, A. Majewska, M. Sur, Dendritic spine dynamics are regulated by monocular deprivation and extracellular matrix degradation. *Neuron* **44**, 1021–1030 (2004).
7. C. J. Shatz, M. P. Stryker, Ocular dominance in layer IV of the cat's visual cortex and the effects of monocular deprivation. *J. Physiol.* **281**, 267–283 (1978).
8. J. A. Gordon, M. P. Stryker, Experience-dependent plasticity of binocular responses in the primary visual cortex of the mouse. *J. Neurosci.* **16**, 3274–3286 (1996).
9. A. E. Takesian, T. K. Hensch, Balancing plasticity/stability across brain development. *Prog. Brain Res.* **207**, 3–34 (2013).
10. Y. Yazaki-Sugiyama *et al.*, Bidirectional plasticity in fast-spiking GABA circuits by visual experience. *Nature* **462**, 218–221 (2009).
11. S. J. Aton *et al.*, Visual experience and subsequent sleep induce sequential plastic changes in putative inhibitory and excitatory cortical neurons. *Proc. Natl. Acad. Sci. U.S.A.* **110**, 3101–3106 (2013).
12. S. J. Kuhlman *et al.*, A disinhibitory microcircuit initiates critical-period plasticity in the visual cortex. *Nature* **501**, 543–546 (2013).
13. T. K. Hensch, M. Fagiolini, Inhibitory threshold for critical-period activation in primary visual cortex. *Nature* **404**, 183–186 (2000).
14. M. Fagiolini *et al.*, Specific GABAA circuits for visual cortical plasticity. *Science* **303**, 1681–1683 (2004).
15. Z. J. Huang *et al.*, BDNF regulates the maturation of inhibition and the critical period of plasticity in mouse visual cortex. *Cell* **98**, 739–755 (1999).
16. U. Rutishauser *et al.*, Activity-dependent PSA expression regulates inhibitory maturation and onset of critical period plasticity. *Nat. Neurosci.* **10**, 1569–1577 (2007).
17. S. Sugiyama *et al.*, Experience-dependent transfer of otx2 homeoprotein into the visual cortex activates postnatal plasticity. *Cell* **134**, 508–520 (2008).
18. Y. Kobayashi, Z. Ye, Takao K. Hensch, Clock genes control cortical critical period timing. *Neuron* **86**, 264–275 (2015).
19. P. Jonas, M. Bartos, I. Vida, Synaptic mechanisms of synchronized gamma oscillations in inhibitory interneuron networks. *Nat. Rev. Neurosci.* **8**, 45–56 (2007).
20. M. A. Whittington *et al.*, Inhibition-based rhythms: Experimental and mathematical observations on network dynamics. *Int. J. Psychophysiol.* **38**, 315–336 (2000).
21. G. Chen *et al.*, Experience-dependent emergence of beta and gamma band oscillations in the primary visual cortex during the critical period. *Sci. Rep.* **5**, 17847–17847 (2015).
22. J. N. MacLean *et al.*, A visual thalamocortical slice. *Nat. Methods* **3**, 129–134 (2006).
23. S. Pangratz-Fuehrer, S. Hestrin, Synaptogenesis of electrical and GABAergic synapses of fast-spiking inhibitory neurons in the neocortex. *J. Neurosci.* **31**, 10767–10775 (2011).
24. Keith B. Hengen *et al.*, Neuronal firing rate homeostasis is inhibited by sleep and promoted by wake. *Cell* **165**, 180–191 (2016).
25. S. Ramaswamy, C. Colangelo, H. Markram, Data-driven modeling of cholinergic modulation of neural microcircuits: Bridging neurons, synapses and network activity. *Front. Neural Circuits* **12**, 77–77 (2018).
26. J. M. Miwa *et al.*, Lynx1, an endogenous toxin-like modulator of nicotinic acetylcholine receptors in the mammalian CNS. *Neuron* **23**, 105–114 (1999).
27. H. Morishita *et al.*, Lynx1, a cholinergic brake, limits plasticity in adult visual cortex. *Science* **330**, 1238–1240 (2010).
28. A. E. Takesian *et al.*, Inhibitory circuit gating of auditory critical-period plasticity. *Nat. Neurosci.* **21**, 218–227 (2018).
29. M. Fagiolini *et al.*, Functional postnatal development of the rat primary visual cortex and the role of visual experience: Dark rearing and monocular deprivation. *Vision Res.* **34**, 709–720 (1994).
30. Y. Iwai *et al.*, Rapid critical period induction by tonic inhibition in visual cortex. *J. Neurosci.* **23**, 6695–6702 (2003).
31. D. Whitteridge, The physiology of nerve cells. By J. C. Eccles. Baltimore: The Johns Hopkins Press. 1957. Pp. ix+270. 30s. *Q. J. Exp. Physiol. Cogn. Med. Sci.* **43**, 133–134 (1958).
32. R. Ge, H. Qian, J.-H. Wang, Physiological synaptic signals initiate sequential spikes at soma of cortical pyramidal neurons. *Mol. Brain* **4**, 19–29 (2011).
33. B. W. Connors, S. J. Cruikshank, T. J. Lewis, Synaptic basis for intense thalamocortical activation of feedforward inhibitory cells in neocortex. *Nat. Neurosci.* **10**, 462–468 (2007).
34. J. R. Geiger *et al.*, Relative abundance of subunit mRNAs determines gating and Ca2+ permeability of AMPA receptors in principal neurons and interneurons in rat CNS. *Neuron* **15**, 193–204 (1995).
35. M. Nahmani, A. Erisir, VGluT2 immunochemistry identifies thalamocortical terminals in layer 4 of adult and developing visual cortex. *J. Comp. Neurol.* **484**, 458–473 (2005).
36. G. O. Sipe *et al.*, Microglial P2Y12 is necessary for synaptic plasticity in mouse visual cortex. *Nat. Commun.* **7**, 10905–10905 (2016).
37. B. Miller, L. Chou, B. L. Finlay, The early development of thalamocortical and corticothalamic projections. *J. Comp. Neurol.* **335**, 16–41 (1993).
38. O. Marin, Thalamocortical topography reloaded: It's not where you go, but how you get there. *Neuron* **39**, 388–391 (2003).
39. A. Agmon *et al.*, Topological precision in the thalamic projection to neonatal mouse barrel cortex. *J. Neurosci.* **15**, 549–561 (1995).
40. D. J. Price *et al.*, The development of cortical connections. *Eur. J. Neurosci.* **23**, 910–920 (2006).
41. S. Rumpel, G. Kattenstroth, K. Gottmann, Silent synapses in the immature visual cortex: Layer-specific developmental regulation. *J. Neurophysiol.* **91**, 1097–1101 (2004).
42. R. K. Reh *et al.*, Critical period regulation across multiple timescales. *Proc. Natl. Acad. Sci. U.S.A.* **117**, 23242–23251 (2020).
43. M. Teleńczuk, B. Teleńczuk, A. Destexhe, Modelling unitary fields and the single-neuron contribution to local field potentials in the hippocampus. *J. Physiol.* **598**, 3957–3972 (2020).
44. B. Teleńczuk *et al.*, Local field potentials primarily reflect inhibitory neuron activity in human and monkey cortex. *Sci. Rep.* **7**, 40211–40211 (2017).
45. M. Bazelot *et al.*, Unitary inhibitory field potentials in the CA3 region of rat hippocampus. *J. Physiol.* **588**, 2077–2090 (2010).
46. A. Citri, R. C. Malenka, Synaptic plasticity: Multiple forms, functions, and mechanisms. *Neuropsychopharmacology* **33**, 18–41 (2008).
47. G. G. Turrigiano, The self-tuning neuron: Synaptic scaling of excitatory synapses. *Cell* **135**, 422–435 (2008).
48. M. C. Chang *et al.*, Narp regulates homeostatic scaling of excitatory synapses on parvalbumin-expressing interneurons. *Nat. Neurosci.* **13**, 1090–1097 (2010).
49. H. Hu, J. Gan, P. Jonas, Fast-spiking, parvalbumin+GABAergic interneurons: From cellular design to microcircuit function. *Science.* **345**, 529–529 (2014).
50. J. S. Haas, C. E. Landisman, Bursts modify electrical synaptic strength. *Brain Res.* **1487**, 140–149 (2012).
51. A. Ribic, M. C. Crair, T. Biederer, Synapse-selective control of cortical maturation and plasticity by parvalbumin-autonomous action of SynCAM 1. *Cell Rep.* **26**, 381–393.e6 (2019).
52. G. Faini *et al.*, Perineuronal nets control visual input via thalamic recruitment of cortical PV interneurons. *Elife* **7**, e41520 (2018).
53. K. K. Lensjø *et al.*, Removal of perineuronal nets unlocks juvenile plasticity through network mechanisms of decreased inhibition and increased gamma activity. *J. Neurosci.* **37**, 1269–1283 (2017).

54. K. Kullander, L. Topolnik, Cortical disinhibitory circuits: Cell types, connectivity and function. *Trends Neurosci.* **44**, 643–657 (2021).
55. S. P. Gandhi, Y. Yanagawa, M. P. Stryker, Delayed plasticity of inhibitory neurons in developing visual cortex. *Proc. Natl. Acad. Sci. U.S.A.* **105**, 16797–16802 (2008).
56. R. A. W. Galuske, M. H. J. Munk, W. Singer, Relation between gamma oscillations and neuronal plasticity in the visual cortex. *Proc. Natl. Acad. Sci. U.S.A.* **116**, 23317–23325 (2019).
57. R. Rodriguez *et al.*, Short- and long-term effects of cholinergic modulation on gamma oscillations and response synchronization in the visual cortex. *J. Neurosci.* **24**, 10369–10378 (2004).
58. M. F. Bear, W. Singer, Modulation of visual cortical plasticity by acetylcholine and noradrenaline. *Nature* **320**, 172–176 (1986).
59. T. Toyoizumi *et al.*, A theory of the transition to critical period plasticity: Inhibition selectively suppresses spontaneous activity. *Neuron* **80**, 51–63 (2013).
60. M. A. Whittington *et al.*, Spatiotemporal patterns of gamma frequency oscillations tetanically induced in the rat hippocampal slice. *J. Physiol.* **502**, 591–607 (1997).
61. P. J. Uhlhaas *et al.*, Neural synchrony and the development of cortical networks. *Trends Cogn. Sci.* **14**, 72–80 (2009).
62. L. J. Benoit *et al.*, Adolescent thalamic inhibition leads to long-lasting impairments in prefrontal cortex function. *Nat. Neurosci.* **25**, 714–725 (2022).
63. N. Gogolla *et al.*, Common circuit defect of excitatory-inhibitory balance in mouse models of autism. *J. Neurodev. Disord.* **1**, 172–181 (2009).
64. K. Q. Do, M. Cuenod, T. K. Hensch, Targeting oxidative stress and aberrant critical period plasticity in the developmental trajectory to schizophrenia. *Schizophr. Bull.* **41**, 835–846 (2015).
65. M. S. Olufsen *et al.*, New roles for the gamma rhythm: Population tuning and preprocessing for the Beta rhythm. *J. Comput. Neurosci.* **14**, 33–54 (2003).
66. Z. F. Mainen, T. J. Sejnowski, Influence of dendritic structure on firing pattern in model neocortical neurons. *Nature* **382**, 363–366 (1996).
67. M. M. McCarthy, Quast-et-al-C++_code. Github. https://github.com/mmccart/Quast-et-al-C--code. Deposited 12 November 2022.